ACS MATERIALS LETTERS

www.acsmaterialsletters.org

LETTER

$Li_2TaS_{1-x}O_xCl_5$: Triple-Anion Glassy Superionic Conductors for High-Performance Solid-State Batteries

Bright O. Ogbolu,[#] Thilina N.D.D. Gamaralalage,[#] Md Mahinur Islam, Tehreem Toheed, Joseph Sariego, Tej P. Poudel, Brian E. Francisco, and Yan-Yan Hu*

Cite This: *ACS Materials Lett.* 2025, 7, 4029–4036

Read Online

ACCESS | Metrics & More | Article Recommendations | Supporting Information

ABSTRACT: **The development of stable, high-performance solid electrolytes is critical for advancing all-solid-state lithium batteries (ASSLBs). We report a series of triple-anion electrolytes, $Li_2TaS_{1-x}O_xCl_5$ ($0 \le x \le 0.9$), synthesized via a rapid 2-hour mechanochemical process. The optimal composition, $Li_2TaS_{0.4}O_{0.6}Cl_5$ (LTSOC), achieves a room-temperature ionic conductivity of ~4.2 mS cm^{-1}, over 15 times that of Li_2TaSCl_5. XRD confirms its amorphous nature, while $^{6/7}$Li NMR reveals one magnetically equivalent lithium environment due to fast ion-exchange dynamics. Raman spectroscopy shows extensive anion mixing within Ta-centered octahedra, where O^{2-} and S^{2-} occupy axial positions, linking Ta−O−S−Cl units, while Li^+ primarily migrates along equatorial Cl^--lined pathways. Nanoindentation reveals a reduced elastic modulus with oxygen incorporation. When employed with commercial NMC811, LTSOC delivers an initial capacity of 187 mAh g^{-1} at 0.1C, with ~81.8% retention after 100 cycles and Coulombic efficiency exceeding 99%. These results demonstrate the promise of amorphous, mixed-anion solid electrolytes for scalable, high-performance ASSLBs.**

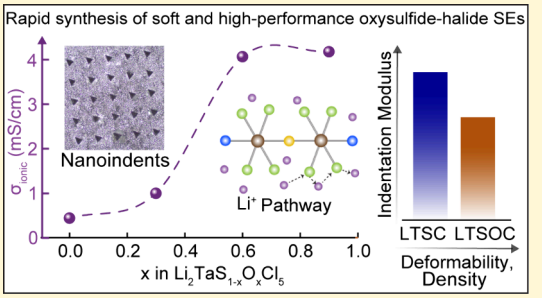

Meeting global decarbonization goals requires energy storage systems that are high-performing, safe, scalable, and sustainable. Lithium-ion batteries are the current standard for portable electronics and are central in the transition toward electric vehicles and renewable energy integration. However, reliance on flammable liquid electrolytes and critical materials like cobalt and nickel raises concerns around safety, cost, and long-term resource availability.[1−3] All-solid-state lithium batteries (ASSLBs), which replace the flammable liquid with an inorganic solid electrolyte (SE), offer a promising alternative with potential for enhanced energy and power density, thermal stability, and improved safety profiles.[4−7]

A key challenge in advancing ASSLBs is developing solid electrolytes (SEs) that combine high lithium-ion conductivity, broad electrochemical stability, mechanical deformability, and scalable synthesis.[8,9] Oxide-based SEs, such as $Li_7La_3Zr_2O_{12}$ and perovskite-type $Li_{0.33}La_{0.55}TiO_3$, exhibit excellent oxidative stability but typically require high-temperature sintering and suffer from interfacial impedance and mechanical rigidity.[10−12] Thiophosphate-based conductors, including $Li_{10}GeP_2S_{12}$ (LGPS) and argyrodite-type Li_6PS_5Cl, offer superionic conductivities exceeding 10 mS cm^{-1} and low interfacial resistance due to their ductility but are limited by poor electrochemical and chemical stability.[13−15] Halide electrolytes such as Li_3InCl_6, Li_3HoCl_6, Li_2ZrCl_6, and Li_3YCl_6 have shown promise with high oxidation stability (up to 4.5 V vs Li^+/Li) and good processability, yet they often exhibit lower conductivities compared to thiophosphates and susceptibility to instability against Li metal anodes.[16−20]

To reconcile the trade-offs among these distinct electrolyte families, mixed-anion strategies have emerged as a promising approach to enhance ionic transport and stability. By combining multiple anionic species with different polarizabilities and bonding preferences, mixed-anion systems introduce local structural disorder, soften the lattice, and enable low-barrier Li-ion conduction pathways.[21−23] Recent work has demonstrated the efficacy of this approach in various binary systems. In $LiNbOCl_4$, corner-sharing oxygen linkages form a flexible framework with low-energy diffusion path-

Received: July 22, 2025
Revised: October 28, 2025
Accepted: November 3, 2025

https://doi.org/10.1021/acsmaterialslett.5c01054
ACS Materials Lett. 2025, 7, 4029−4036

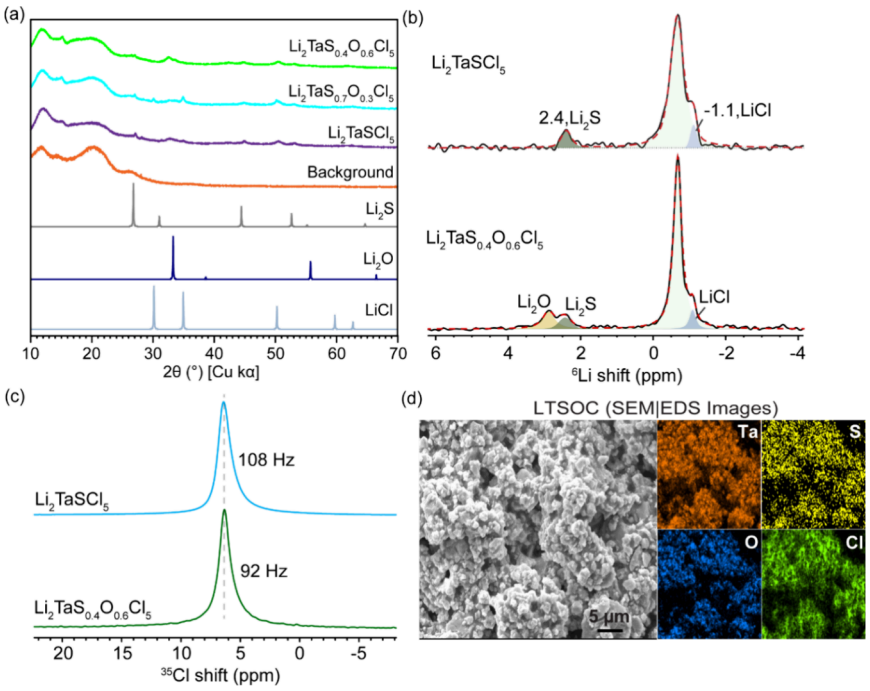

Figure 1. Average structure, local environments, and morphology of the $Li_2TaS_{1-x}O_xCl_5$ series. (a) Powder XRD patterns. (b) ^{6}Li MAS NMR for Li_2TaSCl_5 and $Li_2TaS_{0.4}O_{0.6}Cl_5$. (c) ^{35}Cl MAS NMR spectra showing the halide local environment. (d) Scanning electron microscopy (SEM) images and energy dispersive spectroscopy (EDS) mapping of as-milled $Li_2TaS_{1-x}O_xCl_5$ sample.

ways.[24−26] $LiTaOCl_4$, a highly amorphous material, exhibits superionic properties, though its transport mechanism remains poorly understood.[27−29] Achieving high ionic conductivity in these SEs often requires prolonged high-energy ball milling (10−40 h) or high-temperature sintering to induce disorder or to improve crystallinity.[30,31] These energy- and time-intensive processes hinder scalability. Thus, fast, low-energy routes to produce high-conductivity amorphous halide electrolytes are urgently needed to advance practical ASSLBs.

Here, we investigate a sulfide-halide compound, Li_2TaSCl_5, and introduce a triple mixed-anion system, $Li_2TaS_{1-x}O_xCl_5$ ($0 \leq x \leq 0.9$), designed to combine the key advantages of sulfide, oxide, and halide solid electrolytes within a single disordered framework. The series is synthesized via a rapid, scalable 2 h mechanochemical route, with no evolution of HCl gas commonly reported for analogous oxyhalide systems.[27,30] The optimized composition, $Li_2TaS_{0.4}O_{0.6}Cl_5$ (LTSOC), exhibits a high room-temperature lithium-ion conductivity of ∼4.2 mS cm^{-1}—an order of magnitude improvement over the pristine compound, Li_2TaSCl_5 (LTSC). X-ray diffraction confirms its highly disordered nature, while solid-state $^{6/7}$Li and ^{35}Cl magic-angle-spinning (MAS) NMR reveal a symmetric Cl^- framework and isotropic Li^+ environment with rapid ion exchange. Raman data show a possible clustering of the Cl^-, S^{2-}, and O^{2-} anions around Ta^{5+} centers. This combination of S^{2-}, Cl^-, and O^{2-} anions disrupts long-range ordering and facilitates percolating Li^+ conduction pathways through dynamically reconfigurable local polyhedral environments. Mechanical testing shows that LTSOC deforms more readily and is elastically softer than LTSC. In an all-solid-state Li|LPSC|LTSOC|NMC811 cell, LTSOC is utilized as the catholyte, enabling an initial discharge capacity of ∼187 mAh g^{-1} at 0.1 C (25 °C) and 81.8% capacity retention over 100 cycles with a Coulombic efficiency >99%, demonstrating stable and high performance.

To understand the structural properties of the $Li_2TaS_{1-x}O_xCl_5$ samples prepared via rapid 2-h mechanochemical synthesis, XRD and solid-state MAS NMR were conducted. The XRD patterns of the $Li_2TaS_{1-x}O_xCl_5$ series (Figure 1a) display broad diffraction features, indicative of the lack of a well-defined long-range periodic structure. Despite the broad profile, distinct weak features were detected at approximately 15.1°, 32.6°, and 42.5°. Compared to reference patterns of potential secondary phases, including Li_2S, Li_2O, and LiCl, the Li_2S reflections appear slightly shifted to higher angles by less than 0.5°, particularly in Li_2TaSCl_5 and $Li_2TaS_{0.3}O_{0.7}Cl_5$. Peaks corresponding to Li_2O were observed to be more prominent in $Li_2TaS_{0.4}O_{0.6}Cl_5$.

Additionally, weak reflections near 30° and 50° from LiCl were consistently observed across all samples, likely arising from the intermediate formation of LiCl during the mechanochemical reaction, as similarly reported in related oxyhalide systems.[27,30] The diffraction pattern of the sintered LTSOC sample is shown in Figure S1. While heating produced sharpened peaks with increased crystallinity, it significantly reduced electrochemical performance. The ^{6}Li MAS NMR spectra in Figure 1b provide insight into the local structural environments of Li^+ ions in LTSC and LTSOC. Both samples exhibit near-identical isotropic peaks, −0.67 ppm for LTSC and −0.68 ppm for LTSOC.

Notably, the isotropic ^{6}Li peak resonates close to the LiCl chemical shift at −1.1 ppm, which could stem from possible dominant Li^+-Cl^- interactions. The line width of LTSOC (20 Hz) is over 1.5 times narrower than that of LTSC, 34 Hz. The narrower peak observed in LTSOC suggests (a) a more homogeneous lithium local environment or (b) motional averaging due to faster Li^+ mobility that reduces anisotropic and isotropic broadening.[32−34] The broader line width in LTSC suggests restricted Li^+ ion dynamics. Consistent with

https://doi.org/10.1021/acsmaterialslett.5c01054
ACS Materials Lett. 2025, 7, 4029−4036

the PXRD data, ^{6}Li NMR revealed the presence of minor LiCl and Li_2S impurities in LTSC, and additional Li_2O in LTSOC.

To probe the local Cl^- environment, ^{35}Cl MAS NMR was performed on LTSC and LTSOC. As shown in Figure 1c, both samples exhibit a single sharp ^{35}Cl resonance centered at ~6.4 ppm, indicating that Cl^- ions experience a comparable local coordination environment. The retention of a similar chemical shift between the two materials confirms that Cl^- remains structurally integrated into the mixed-anion framework, likely within the Ta-centered octahedra, and not phase-separated or forming LiCl-like domains, except for the minor LiCl impurities observed. The ^{35}Cl peak in LTSOC is narrower (92 Hz) compared to that in LTSC (108 Hz). Enhanced Li^+ or anion dynamics in LTSOC could contribute to motional averaging of the quadrupolar interaction, yielding narrowed lines. These results complement the ^{6}Li NMR data discussed previously and reinforce the notion that oxygen substitution modulates the local anion framework, thereby facilitating dynamic environments conducive to fast ion transport.

SEM and EDS analyses were performed on ball-milled LTSOC (Figure 1d) and LTSC (Figure S2) powders to assess their morphology and elemental distribution. SEM images show that LTSOC particles exhibit more aggregation than those of LTSC, indicative of enhanced interparticle contact. EDS maps confirm a uniform distribution of Ta, S, O, and Cl in LTSOC, indicating successful integration of all anions into the amorphous matrix. Similarly, LTSC displays homogeneous mapping of Ta, S, and Cl.

Figure 2a presents the Raman spectra of several tantalum-based compounds and the synthesized LTSOC: $TaCl_5$, $LiTaCl_6$, Ta_2O_5, and $Li_2TaS_{0.4}O_{0.6}Cl_5$. The spectrum of $TaCl_5$ exhibits sharp peaks, typical of molecular species. The bands between 100 and 200 cm^{-1} originate from Ta−Cl bending modes; specifically, those below 150 cm^{-1} arise from out-of-plane bending due to Cl wagging or twisting, and those between 150 and 200 cm^{-1} from in-plane Cl bending. The peaks between 200 and 400 cm^{-1} are attributed to Ta−Cl stretching, including the intense, sharp peak at ~405 cm^{-1} from axial Ta−Cl symmetric stretch and the weaker peaks at slightly lower wavenumbers from equatorial Ta−Cl symmetric stretch. $LiTaCl_6$ shows similar peaks but slightly broader with lower intensity, typical of extended 3D lattices with long-range interactions, lattice vibrations, and possible site disorder. In contrast, the spectrum of LTSOC (red curve) shows significantly broadened peaks and notable shifts, indicating substantial structural modification due to partial substitution of S^{2-} and O^{2-} for Cl^- within the $[TaS_xO_{1-x}Cl_5]^{2-}$ octahedra. Figure 2b provides a more detailed view of the Raman features for LTSOC. Low-wavenumber peaks at approximately 134 cm^{-1} and 165 cm^{-1} are assigned to Ta−Cl and Ta−S bending vibrations.[35] The low resolution of these bending modes in the Raman spectrum indicates heterogeneity in the local structure and bonding environments. A broad, prominent peak at ~330 cm^{-1}, absent in $TaCl_5$ and $LiTaCl_6$, is attributed to a Cl−Ta−S vibrational mode, potentially arising from a hybrid Cl−Ta−S linkage or structural distortions induced by multianion coordination. This peak is flanked by the Ta−S E_g mode at ~300 cm^{-1},[36,37] and the octahedral Ta−Cl A_{1g} mode at ~405 cm^{-1}. This assignment is consistent with literature reports attributing Ta−S vibrations in the 260−390 cm^{-1} range for related compounds with Ta−S−Ta linkages.[38−42] Notably, this 405 cm^{-1} peak from axial Ta−Cl symmetric stretching—dominant in $TaCl_5$—is significantly diminished in LTSOC, indicating that S/O substitution mainly occurs at axial positions, as illustrated in Figure 2b. In the 600−900 cm^{-1} region (highlighted in blue), the LTSOC spectrum shows broad features associated with oxygen incorporation, specifically Ta−O−Ta stretching and bending modes.[43] These features confirm the presence of Ta−O bonds. The broadening across the spectrum reflects increased structural disorder, which is likely to influence ionic transport properties.

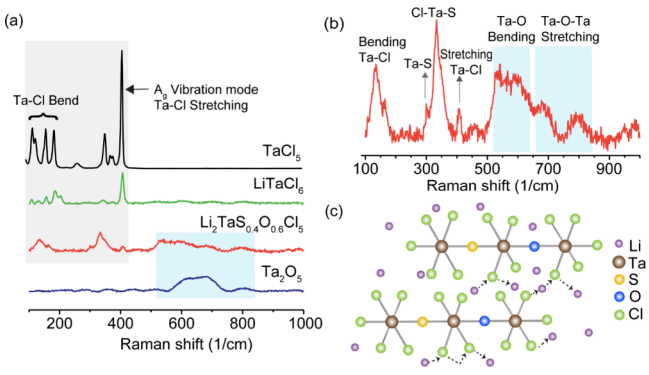

Figure 2. Raman spectra and short-range structural analysis of $Li_2TaS_{0.4}O_{0.6}Cl_5$. (a) Comparison with reference compounds. (b) Raman spectrum of $Li_2TaS_{0.4}O_{0.6}Cl_5$ with key vibrational modes assigned. (c) Polymeric-type $[TaS_xO_{1-x}Cl_5]^{2-}$ anionic chains with possible Li^+−Cl^- interactions along the conduction pathways indicated.

The anion arrangement shown in Figure 2c aligns with the basic structural motifs reported for compounds such as $LiTaOCl_4$ and $LiNbOCl_4$, in which the M^{5+} octahedra $[MO_2Cl_4]$ are coordinated equatorially by four Cl^- ions and axially by two O^{2-} atoms. These axial oxygens bridge neighboring Ta/Nb centers along the c-direction, forming 1D flexible anionic chains.[24,30,44] Similarly, the placement of S^{2-} into axial O^{2-} positions is consistent with computational studies on the $[TaSOCl_4]$ octahedron, where sulfur preferentially occupies axial sites due to its lower substitution free energy (ΔG)—over 26 times lower for S replacing O compared to Cl.[27]

Figure 2c schematically illustrates short-range ordered motifs and possible Li^+ diffusion pathways. The Ta-centered octahedra are connected into polymeric chains, forming a symmetrical, yet locally disordered anion environment composed of S, O, and Cl. The dashed lines indicate potential Li^+ hopping pathways. Li^+ diffusion in the amorphous LTSOC phase likely proceeds via localized hops between coordination sites in the distorted [Ta−Cl−O−S] clusters. These clusters generate a dynamic energy landscape, with Li^+ ions interacting weakly, particularly with Cl^-, as supported by ^{6}Li NMR, which shows proximity to halide-rich environments. This mechanism is reminiscent of the "monkey-bar" transport model proposed for $LiTaCl_6$ by Lei et al.,[45] where Li^+ ions transiently coordinate to anionic sites before hopping to the next site. Such sequential hopping creates a percolating network of migration pathways, enabling long-range ionic conduction even in the absence of long-range crystalline order. The bridging O and S links $[TaS_xO_{1-x}Cl_5]$ octahedra, which may facilitate Li^+ hopping between different $[TaS_xO_{1-x}Cl_5]$ octahedron units and promote long-range Li^+ diffusion with high transference numbers.

https://doi.org/10.1021/acsmaterialslett.5c01054
ACS Materials Lett. 2025, 7, 4029−4036

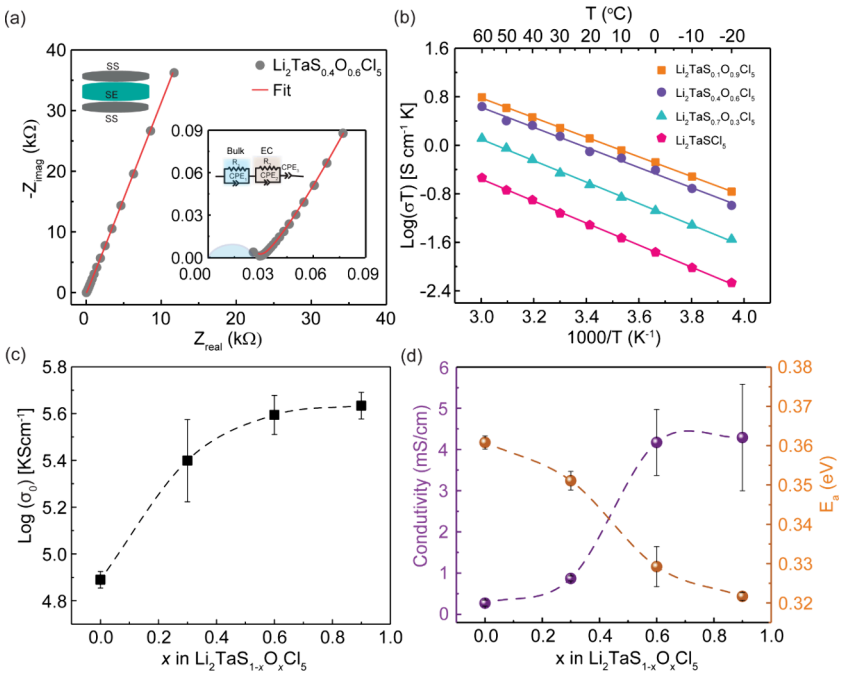

Figure 3. Electrochemical properties of $Li_2TaS_{1-x}O_xCl_5$. (a) Nyquist plots and equivalent circuit fit of $Li_2TaS_{0.4}O_{0.6}Cl_5$ at 25 °C. (b) Arrhenius plots of the $Li_2TaS_{1-x}O_xCl_5$ series measured from −20 to 60 °C. (c) Arrhenius prefactor (σ_0) distribution in the LTSOC series. (d) Comparison of the ionic conductivities and activation energies trend in the $Li_2TaS_{1-x}O_xCl_5$ series. Data points with error bars represent means and standard deviations ($x \pm 1\sigma$) from measurements conducted on three or more samples.

The room-temperature ^{7}Li T_1 spin−lattice relaxation times for the LTSOC and LTSC are approximately 0.45 and 0.25 s, respectively (Figure S3). The longer T_1 in the oxygen-rich LTSOC suggests slower relaxation. To relate these relaxation behaviors to ion mobility and determine the motional regime, the Bloembergen−Purcell−Pound (BPP) model[46] was applied to variable-temperature T_1 measurements (Figure S3a, Tables S1 and S2). Both LTSC and LTSOC exhibit trends characteristic of the slow-to-intermediate motion regime, in which higher Li^+ mobility leads to shorter T_1 times before T_1 reaches the minimum.[46] Thus, shorter T_1 times in the slow motional regime typically correlate with faster Li^+ motion. However, the observed discrepancy between the absolute T_1 values for LTSOC and LTSC and the conductivity trend (discussed in the next section) implies that Li^+ jump frequency alone may not fully explain the superionic behavior observed in LTSOC. Other factors, may contribute to the observed high ionic conductivity.

Additionally, the ^{7}Li MAS NMR spectra (Figure S3b) show a clear temperature-dependent line width narrowing in both LTSC and LTSOC, indicative of enhanced Li^+ mobility at elevated temperatures. In LTSC, the line width decreases from 648 Hz at 25 °C to 480 Hz at 85 °C, while in LTSOC, it narrows from 460 to 360 Hz. This behavior reflects thermally activated Li^+ motion and motional averaging of residual ^{7}Li−^{7}Li dipolar coupling interactions.

The ionic transport properties of LTSOC were evaluated using temperature-dependent electrochemical impedance spectroscopy. At 25 °C, the fitted Nyquist plot (Figure 3a) yields a total ionic conductivity of ∼4.2 mS cm^{-1}. The data were modeled using an equivalent circuit (inset, Figure 3a), consisting of a parallel resistor and constant phase element (R, CPE) to represent the ionic response of the sample, in series with a second CPE that accounts for the ion-blocking behavior of the stainless-steel electrodes. The extracted Brug capacitance (∼10^{-11} F) suggests the contributions from bulk and grain boundaries cannot be clearly distinguished. Even at −20 °C (Figure S4), the impedance response does not resolve separate features for bulk and grain boundary processes. As such, the reported values reflect total ionic conductivity, consistent with trends observed in related halide-based solid electrolytes.[47,48]

Arrhenius plots for the $Li_2TaS_{1-x}O_xCl_5$ series derived from variable-temperature EIS measurements (Figure S5) are presented in Figure 3b, with the corresponding activation energies and room-temperature ionic conductivities, calculated using eqs S1 and S2, summarized in Figure 3d. The unsubstituted LTSC exhibits the highest activation energy (∼0.36 eV) and the lowest conductivity (0.27 mS cm^{-1}). In contrast, partial substitution of S^{2-} with O^{2-} significantly enhances conductivity, with values reaching 0.87, 4.17, and 4.29 mS cm^{-1} for x = 0.3, 0.6, and 0.9, respectively. This increase is accompanied by a corresponding decrease in activation energy to 0.35, 0.33, and 0.32 eV, respectively. Notably, no significant difference in conductivity is observed between the x = 0.6 and x = 0.9 compositions. Oxygen incorporation likely stabilizes a superionic phase, as $Li_2TaS_{0.4}O_{0.6}Cl_5$ exhibits a more than 15-fold improvement in conductivity compared to LTSC. With a total processing time under 2.5 h, this mechanochemically synthesized LTSOC material compares favorably with most reported lithium halide fast-ion conductors synthesized through lengthy, multistep, or high-temperature processes.

In Figure 3c, we observe a systematic increase in log(σ_0) with increasing oxygen content (x) in $Li_2TaS_{1-x}O_xCl_5$, particularly from x = 0 to 0.6, before reaching a plateau. This rise in the prefactor σ_0, which includes an entropic component through the term exp($\Delta S_m/k_B$),[50] reflects a higher entropy of migration, S_m, driven by increased structural and

https://doi.org/10.1021/acsmaterialslett.5c01054
ACS Materials Lett. 2025, 7, 4029−4036

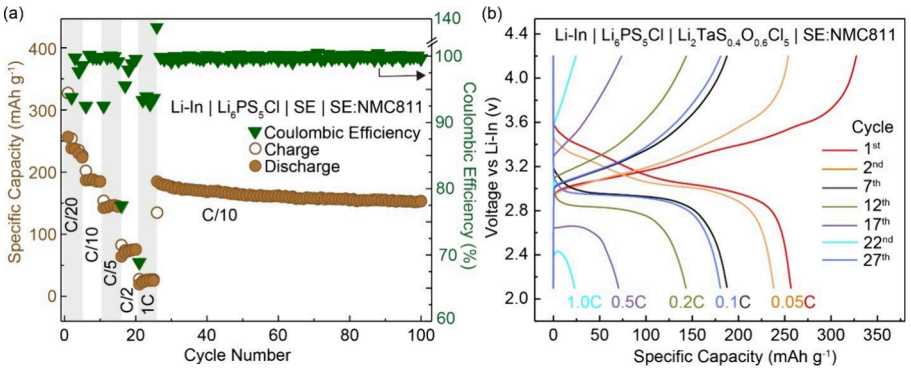

Figure 4. All-solid-state battery cycling performance of $Li_2TaS_{0.4}O_{0.6}Cl_5$ in a cell with the configuration of Li−In|Li_6PS_5Cl|SE|SE:NMC811(1:1), where SE is $Li_2TaS_{0.4}O_{0.6}Cl_5$. (a) Rate capability plots. (b) Voltage-capacity profiles showing the charge−discharge curves at 0.05C, 0.1C, 0.2C, 0.5C, and 1C. C = 275.5 mAh g^{-1}, referenced to the theoretical capacity of NMC811.[49]

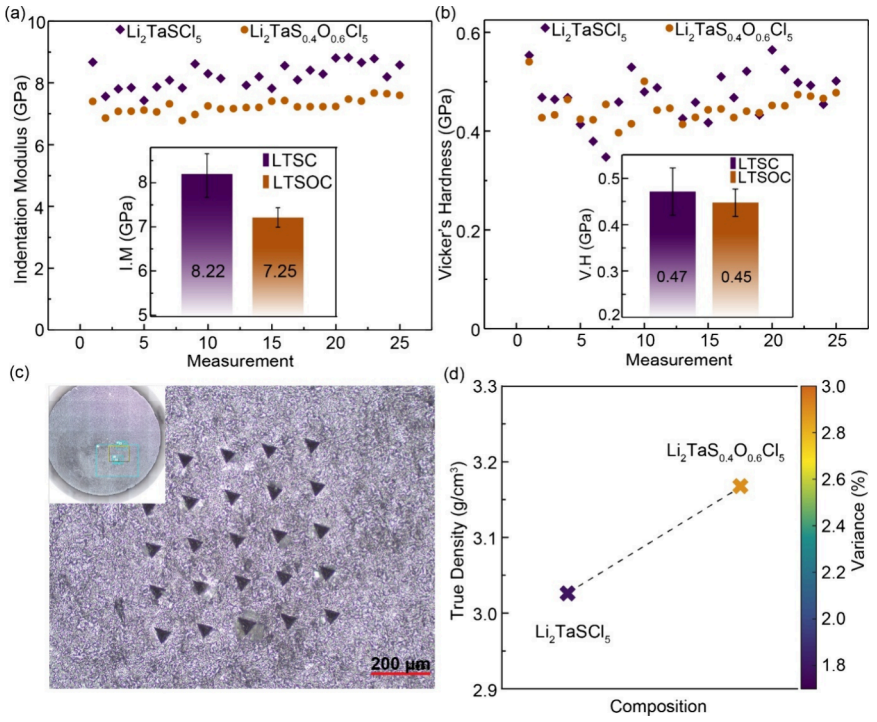

Figure 5. Mechanical properties of Li_2TaSCl_5 and $Li_2TaS_{0.4}O_{0.6}Cl_5$. (a) Indentation modulus measured using the Advanced Dynamic Modulus and Hardness (ADEH) protocol. (b) Vickers hardness values. The error bars represent the standard deviation ($x \pm 1\sigma$) of multiple measurements. (c) Optical surface profilometry images (10× magnification) of a 5 × 5 grid of indentation points (depth 4−5 μm) on a $Li_2TaS_{0.4}O_{0.6}Cl_5$ pellet. Inset: Pellet image at 2.5× magnification, with marked areas showing the indented sections. (d) True density measurements by gas pycnometry.

dynamic disorder introduced by oxygen substitution. The resulting entropic enhancement complements the reduction in activation energy and contributes to the overall improvement in ionic conductivity. Figure S6 shows the current−time response at various voltages, with the inset displaying the corresponding I−V plot. From this, the electronic conductivity of LTSOC was determined to be ~3 × 10^{-9} S cm^{-1}, confirming its negligible contribution to the total conductivity of 4.2 mS cm^{-1}. These results underscore the potential of triple-anion design for enabling high-performance solid electrolytes compatible with large-scale solid-state battery manufacturing.

ASSLBs assembled using the commercially available high-voltage NMC811 cathode and a multilayered configuration NMC811:LTSOC|LTSOC|Li_6PS_5Cl|Li−In were cycled between 2.1 and 4.2 V at 23 °C. To evaluate rate capability, initial cycles were performed at 0.05C, 0.1C, 0.2C, 0.5C, and 1C (C = 275.5 mAh g^{-1}), delivering discharge capacities of 256.7, 187.0, 143.4, 70.4, and 23.0 mAh g^{-1}, respectively (Figure 4a). The decline in capacity with increasing C-rate reflects kinetic limitations, including sluggish Li^+ transport and elevated overpotential. At higher current densities, increased ionic flux and restricted charge transfer induce greater polarization, leading to early voltage cutoffs and under-utilization of the cathode.[49] These effects are also evident in the voltage profiles (Figure 4b), which show modest hysteresis that gradually widens with cycling, likely due to an increase in overpotential at high rates.

Despite these challenges, the cell maintains excellent long-term stability, retaining 152.9 mAh g^{-1} over 100 cycles at

https://doi.org/10.1021/acsmaterialslett.5c01054
ACS Materials Lett. 2025, 7, 4029−4036

0.1C—approximately 81.8% of its initial capacity. This performance is attributed to (i) the chemical and electrochemical compatibility of LTSOC with NMC811, which minimizes parasitic reactions and promotes a stable cathode-electrolyte interphase (CEI),(ii) the high oxidative stability of LTSOC, preventing electrolyte breakdown at elevated voltages,and (iii) maintenance of good cathode-electrolyte interfacial contact due to favorable mechanical properties of the glassy triple-anion conductor. As a result, a high Coulombic efficiency of >99% is maintained throughout long-term cycling. These results demonstrate LTSOC as a promising high-voltage-compatible solid electrolyte for enabling durable solid-state batteries.

Given the role of mechanical features in sustaining cathode-electrolyte contact, we characterized the mechanical response of the glassy triple-anion conductor. Figure 5a and 5b show the indentation modulus and Vickers hardness of both SEs, measured using a Berkovich nanoindenter. Indentation hardness (converted to Vickers hardness, see methods in the Supporting Information) quantifies how resistant a material is to permanent plastic deformation under a sharp indenter, whereas indentation modulus reflects the elastic response of a material, derived from the contact stiffness normalized by contact area.[51] At depths of 4−5 μm, we find that LTSC exhibits a higher indentation modulus (∼8.2 GPa) compared to LTSOC (∼7.3 GPa), a ∼12% decrease upon O^{2-} substitution. A lower indentation modulus for LTSOC means that the material is elastically softer or less stiff under load. This could be beneficial for maintaining good interfacial contact with electrodes and for accommodating volumetric changes during battery cycling.[52] Hardness values, by contrast, were not significantly different, with LTSC having a slightly higher Vickers hardness of ∼0.47 and LTSOC ∼0.45 GPa (Figure 5b). The overlap within experimental scatter suggests that oxygen incorporation does not significantly alter the plastic resistance to indentation. Their hardness (0.4−0.5 GPa) is consistent with halide SEs, and far lower than garnet oxides such as $Li_7La_3Zr_2O_{12}$ (>6 GPa hardness, modulus >150 GPa).[52−54]

Figure 5c presents optical images of the indented LTSOC pellet surface, confirming reproducible indentation imprints without major crack formation or delamination. The absence of severe cracking indicates that these electrolytes can undergo localized deformation under stress. True density measurements (Figure 5d) confirm that the lower modulus of LTSOC is intrinsic and not due to porosity effects. LTSOC exhibits a higher density (3.17 g cm^{-3}) than LTSC (3.03 g cm^{-3}), with relatively low variance (2.9%).

In conclusion, we investigated the structure and performance of a series of superionic solid electrolytes, $Li_2TaS_{1-x}O_xCl_5$ ($0 \leq x \leq 0.9$), synthesized via a 2-h mechanochemical route. The composition, $Li_2TaS_{0.4}O_{0.6}Cl_5$, achieved a room-temperature ionic conductivity of ∼4.2 mS cm^{-1} with a low activation energy of ∼0.33 eV, representing a ∼15-fold enhancement compared to Li_2TaSCl_5. XRD confirmed their amorphous nature, while $^{6/7}$Li NMR revealed fast-moving Li^+ ions interacting with Cl^-. Raman spectra showed broadened and weakened Ta−Cl vibrational modes and new modes associated with Ta−O and Ta−S bonding, with O^{2-} and S^{2-} occupying axial sites and bridging [$TaSOCl_4$] octahedra, facilitating Li^+ transport across units. An all-solid-state battery employing $Li_2TaS_{0.4}O_{0.6}Cl_5$ as the catholyte and NMC811 as the cathode delivered an initial specific capacity of ∼187 mAh g^{-1}, retained ∼81.8% capacity after 100 cycles at 0.1C, and exhibited >99% Coulombic efficiency. Nanoindentation confirmed that oxygen substitution lowers modulus while preserving hardness, yielding mechanical compliance for stable interfaces. These results highlight the critical role of oxygen incorporation in stabilizing a fast-ion-conducting disordered structure, providing a generalizable design strategy for high-performance, scalable halide-based SEs for next-generation ASSLBs.

■ ASSOCIATED CONTENT

Data Availability Statement

Data supporting the findings of this study are available from the corresponding author upon request.

Supporting Information

The Supporting Information is available free of charge at https://pubs.acs.org/doi/10.1021/acsmaterialslett.5c01054.

Detailed experimental procedures, materials, and methods, and additional data, including selected XRD patterns, SEM images, NMR T_1 relaxation data, EIS data, and DC polarization data (PDF)

■ AUTHOR INFORMATION

Corresponding Author

Yan-Yan Hu − *Department of Chemistry and Biochemistry, Florida State University, Tallahassee, Florida 32306, United States; Materials Science and Engineering Program, Florida State University, Tallahassee, Florida 32310, United States; Center of Interdisciplinary Magnetic Resonance, National High Magnetic Field Laboratory, Tallahassee, Florida 32310, United States;* orcid.org/0000-0003-0677-5897; Email: yhu@fsu.edu

Authors

Bright O. Ogbolu − *Department of Chemistry and Biochemistry, Florida State University, Tallahassee, Florida 32306, United States*

Thilina N.D.D. Gamaralalage − *Department of Chemistry and Biochemistry, Florida State University, Tallahassee, Florida 32306, United States*

Md Mahinur Islam − *Department of Chemistry and Biochemistry, Florida State University, Tallahassee, Florida 32306, United States*

Tehreem Toheed − *Department of Chemistry and Biochemistry, Florida State University, Tallahassee, Florida 32306, United States*

Joseph Sariego − *Solid Power, Inc., Louisville, Colorado 80027, United States*

Tej P. Poudel − *Materials Science and Engineering Program, Florida State University, Tallahassee, Florida 32310, United States*

Brian E. Francisco − *Solid Power, Inc., Louisville, Colorado 80027, United States*

Complete contact information is available at: https://pubs.acs.org/10.1021/acsmaterialslett.5c01054

Author Contributions

#B.O.O. and T.N.D.D.G. contributed equally. CRediT: **Bright Ogbolu** data curation, formal analysis, investigation, visualization, writing - original draft; **Thilina Nadeemali Dikella Dikella Gamaralalage** data curation, formal analysis, investigation, visualization, writing - original draft; **Md Mahinur Islam** data curation, investigation; **Tehreem Toheed** data

https://doi.org/10.1021/acsmaterialslett.5c01054
ACS Materials Lett. 2025, 7, 4029−4036

curation, investigation; **Joseph Sariego** data curation, formal analysis, investigation,writing-original draft; **Tej Prasad Poudel** visualization; **Brian E Francisco** methodology, resources, supervision, validation,writing-review & editing; **Yan-Yan Hu** conceptualization, methodology, funding acquisition, project administration, supervision, formal analysis, validation, writing - review & editing.

Notes

The authors declare no competing financial interest.

■ ACKNOWLEDGMENTS

This work was supported by the National Science Foundation (NSF) under grant no. DMR-1847038. Solid-state NMR measurements were carried out at the National High Magnetic Field Laboratory, supported by NSF Cooperative Agreements DMR-1644779 and DMR-2128556, and the State of Florida. This research includes Raman experiments provided by the Materials Characterization Laboratory at the Florida State University Department of Chemistry and Biochemistry (FSU075000MAC), with technical assistance provided by Dr. Raaj Winfred.

■ REFERENCES

(1) Manthiram, A. A. Reflection on Lithium-Ion Battery Cathode Chemistry. *Nat. Commun.* **2020**, *11*, 1550.
(2) Kmiec, S.; Ruoff, E.; Manthiram, A. A New Class of Oxyhalide Solid Electrolytes $NaNbCl_{6-2x}O_x$ for Solid-State Sodium Batteries. *Angew. Chem., Int. Ed.* **2025**, *64*, No. e202416979.
(3) Manthiram, A. An Outlook on Lithium-Ion Battery Technology. *ACS Cent. Sci.* **2017**, *3*, 1063−1069.
(4) Janek, J.; Zeier, W. G. A Solid Future for Battery Development. *Nat. Energy* **2016**, *1*, 16141.
(5) Sun, Y. K. Promising All-Solid-State Batteries for Future Electric Vehicles. *ACS Energy Lett.* **2020**, *5*, 3221−3223.
(6) Liang, J.; Li, X.; Wang, C.; Kim, J. T.; Yang, R.; Wang, J.; Sun, X. Current Status and Future Directions in Environmental Stability of Sulfide Solid-State Electrolytes for All-Solid-State Batteries. *Energy Mater. Adv.* **2023**, *4*, 0021.
(7) Yang, J.; Lin, J.; Brezesinski, T.; Strauss, F. Emerging Superionic Sulfide and Halide Glass-Ceramic Solid Electrolytes: Recent Progress and Future Perspectives. *ACS Energy Lett.* **2024**, *9*, 5977−5990.
(8) Janek, J.; Zeier, W. G. Challenges in Speeding up Solid-State Battery Development. *Nat. Energy* **2023**, *8*, 230−240.
(9) Schmaltz, T.; Hartmann, F.; Wicke, T.; Weymann, L.; Neef, C.; Janek, J. A Roadmap for Solid-State Batteries. *Adv. Energy Mater.* **2023**, *13*, 2301886.
(10) Kuhn, A.; Narayanan, S.; Spencer, L.; Goward, G.; Thangadurai, V.; Wilkening, M. Li Self-Diffusion in Garnet-Type Li7La3Zr 2O12 as Probed Directly by Diffusion-Induced Li7 Spin-Lattice Relaxation NMR Spectroscopy. *Phys. Rev. B* **2011**, *83*, 094302.
(11) Han, J.; Zhu, J.; Li, Y.; Yu, X.; Wang, S.; Wu, G.; Xie, H.; Vogel, S. C.; Izumi, F.; Momma, K.; Kawamura, Y.; Huang, Y.; Goodenough, J. B.; Zhao, Y. Experimental Visualization of Lithium Conduction Pathways in Garnet-Type Li7La3Zr2O12. *Chem. Commun.* **2012**, *48*, 9840−9842.
(12) Huang, Y.; Liu, X.; Jiang, Y.; Zhu, X. Synthesis of Textured Li0.33La0.55TiO3 Solid Electrolytes by Molten Salt Method. *Ceram. Int.* **2021**, *47*, 11654−11661.
(13) Gorai, P.; Long, H.; Jones, E.; Santhanagopalan, S.; Stevanović, V. Defect Chemistry of Disordered Solid-State Electrolyte Li10-GeP2S12. *J. Mater. Chem. A* **2020**, *8*, 3851−3858.
(14) Feng, X.; Chien, P. H.; Wang, Y.; Patel, S.; Wang, P.; Liu, H.; Immediato-Scuotto, M.; Hu, Y. Y. Enhanced Ion Conduction by Enforcing Structural Disorder in Li-Deficient Argyrodites Li6-xPS5-xCl1+x. *Energy Storage Mater.* **2020**, *30*, 67−73.
(15) Weber, D. A.; Senyshyn, A.; Weldert, K. S.; Wenzel, S.; Zhang, W.; Kaiser, R.; Berendts, S.; Janek, J.; Zeier, W. G. Structural Insights and 3D Diffusion Pathways within the Lithium Superionic Conductor Li10GeP2S12. *Chem. Mater.* **2016**, *28*, 5905−5915.
(16) Park, K. H.; Kaup, K.; Assoud, A.; Zhang, Q.; Wu, X.; Nazar, L. F. High-Voltage Superionic Halide Solid Electrolytes for All-Solid-State Li-Ion Batteries. *ACS Energy Lett.* **2020**, *5*, 533−539.
(17) Kim, K.; Park, D.; Jung, H. G.; Chung, K. Y.; Shim, J. H.; Wood, B. C.; Yu, S. Material Design Strategy for Halide Solid Electrolytes Li3MX6(X = Cl, Br, and I) for All-Solid-State High-Voltage Li-Ion Batteries. *Chem. Mater.* **2021**, *33*, 3669−3677.
(18) Li, X.; Liang, J.; Yang, X.; Adair, K. R.; Wang, C.; Zhao, F.; Sun, X. Progress and Perspectives on Halide Lithium Conductors for All-Solid-State Lithium Batteries. *Energy Environ. Sci.* **2020**, *13*, 1429−1461.
(19) Riegger, L. M.; Schlem, R.; Sann, J.; Zeier, W. G.; Janek, J. Lithium-Metal Anode Instability of the Superionic Halide Solid Electrolytes and the Implications for Solid-State Batteries. *Angew. Chem., Int. Ed.* **2021**, *60*, 6718−6723.
(20) Ogbolu, B. O.; Poudel, T. P.; Dikella, T. N. D. D.; Truong, E.; Chen, Y.; Hou, D.; Li, T.; Liu, Y.; Gabriel, E.; Xiong, H.; Huang, C.; Hu, Y. Y. Tailoring Ion Transport in $Li_{3-3y}Ho_{1+y}Cl_{6-X}Br_x$ via Transition-Metal Free Structural Planes and Charge Carrier Distribution. *Adv. Sci.* **2025**, *12*, 2409668.
(21) Park, K.-H.; Kim, S. Y.; Jung, M.; Lee, S.-B.; Kim, M.-J.; Yang, I.-J.; Hwang, J.-H.; Cho, W.; Chen, G.; Kim, K.; Yu, J. Anion Engineering for Stabilizing Li Interstitial Sites in Halide Solid Electrolytes for All-Solid-State Li Batteries. *ACS Appl. Mater. Interfaces* **2023**, *15*, 58367−58376.
(22) Huang, L.; Barker, K.; Liu, X.; Jian, Y.; Skinner, S. J.; Ryan, M. P.; Huang, C. A Mixed-Anion Strategy for Constructing Rapid Ion-Conducting Na Solid-State Electrolyte. *Chem. Inorg. Mater.* **2025**, *6*, 100102.
(23) Shen, L.; Li, J. L.; Kong, W. J.; Bi, C. X.; Xu, P.; Huang, X. Y.; Huang, W. Z.; Fu, F.; Le, Y. C.; Zhao, C. Z.; Yuan, H.; Huang, J. Q.; Zhang, Q. Anion-Engineering Toward High-Voltage-Stable Halide Superionic Conductors for All-Solid-State Lithium Batteries. *Adv. Funct. Mater.* **2024**, *34*, 2408571.
(24) Adams, S. Origin of Fast Li+-Ion Conductivity in the Compressible Oxyhalide LiNbOCl4. *Energy Storage Mater.* **2024**, *68*, 103359.
(25) Singh, B.; Wang, Y.; Liu, J.; Bazak, J. D.; Shyamsunder, A.; Nazar, L. F. Critical Role of Framework Flexibility and Disorder in Driving High Ionic Conductivity in LiNbOCl4. *J. Am. Chem. Soc.* **2024**, *146*, 17158−17169.
(26) Jeon, S.; Park, K.-H.; Cho, W.; Jeong, G.; Yu, J.; Park, Y. J.; Kim, K. Hydrochloric Acid-Free Synthesis of LiNbOCl4 Superionic Conductor for All-Solid-State Li Batteries. *Solid State Ionics* **2025**, *421*, 116791.
(27) Li, L.; Jiang, Z.; Yang, J.; Liu, C.; Luo, Q.; Li, S.; Zhang, L.; Chen, X.; Cheng, S.; Yu, C. A Rapid Synthesis of Amorphous LiTaOCl4 Solid Electrolytes Through a Two-Step Reaction Pathway for High-Rate and Long-Cycling Lithium Batteries. *Adv. Funct. Mater.* **2025**, *35*, 2410008.
(28) Zhang, S.; Zhao, F.; Chang, L. Y.; Chuang, Y. C.; Zhang, Z.; Zhu, Y.; Hao, X.; Fu, J.; Chen, J.; Luo, J.; Li, M.; Gao, Y.; Huang, Y.; Sham, T. K.; Gu, M. D.; Zhang, Y.; King, G.; Sun, X. Amorphous Oxyhalide Matters for Achieving Lithium Superionic Conduction. *J. Am. Chem. Soc.* **2024**, *146*, 2977−2985.
(29) Zhang, S.; Zhao, F.; Chen, J.; Fu, J.; Luo, J.; Alahakoon, S. H.; Chang, L. Y.; Feng, R.; Shakouri, M.; Liang, J.; Zhao, Y.; Li, X.; He, L.; Huang, Y.; Sham, T. K.; Sun, X. A Family of Oxychloride Amorphous Solid Electrolytes for Long-Cycling All-Solid-State Lithium Batteries. *Nat. Commun.* **2023**, *14*, 3780.
(30) Tanaka, Y.; Ueno, K.; Mizuno, K.; Takeuchi, K.; Asano, T.; Sakai, A. New Oxyhalide Solid Electrolytes with High Lithium Ionic Conductivity > 10 mS/cm for All-Solid-State Batteries. *Angew. Chem., Int. Ed.* **2023**, *62*, 14073.

https://doi.org/10.1021/acsmaterialslett.5c01054
ACS Materials Lett. 2025, 7, 4029−4036

(31) Zhao, T.; Samanta, B.; de Irujo-Labalde, X. M.; Whang, G.; Yadav, N.; Kraft, M. A.; Adelhelm, P.; Hansen, M. R.; Zeier, W. G. Sodium Metal Oxyhalides NaMOCl4 (M = Nb, Ta) with High Ionic Conductivities. *ACS Mater. Lett.* **2024**, *6*, 3683−3689.
(32) Chien, P.-H.; Griffith, K. J.; Liu, H.; Gan, Z.; Hu, Y.-Y. Recent Advances in Solid-State Nuclear Magnetic Resonance Techniques for Materials Research. *Annu. Rev. Mater. Res.* **2020**, *50*, 493−520.
(33) Helm, B.; Minafra, N.; Wankmiller, B.; Agne, M. T.; Li, C.; Senyshyn, A.; Hansen, M. R.; Zeier, W. G. Correlating Structural Disorder to Li+Ion Transport in $Li_{4-X}Ge_{1-X}Sb_xS_4$ ($0 \leq x \leq 0.2$). *Chem. Mater.* **2022**, *34*, 5558−5570.
(34) Wu, N.; Chien, P. H.; Li, Y.; Dolocan, A.; Xu, H.; Xu, B.; Grundish, N. S.; Jin, H.; Hu, Y. Y.; Goodenough, J. B. Fast Li+ Conduction Mechanism and Interfacial Chemistry of a NASICON/Polymer Composite Electrolyte. *J. Am. Chem. Soc.* **2020**, *142* (5), 2497−2505.
(35) York, N.; King, C.; Huglen, R.; Poulsen, F. W.; Mamantov, G.; Begun, G. M. *The Principles of Inorganic Chemistry*; Academic Press: 1969.
(36) Yanase, T.; Ebashi, M.; Takamure, K.; Ise, W.; Waizumi, H.; Chikamatsu, A.; Hirose, Y.; Shimada, T. Unidirectional Growth of Epitaxial Tantalum Disulfide Triangle Crystals Grown on Sapphire by Chemical Vapour Deposition with a Separate-Flow System. *CrystEngComm* **2024**, *26*, 341−348.
(37) Zhao, R.; Grisafe, B.; Ghosh, R. K.; Holoviak, S.; Wang, B.; Wang, K.; Briggs, N.; Haque, A.; Datta, S.; Robinson, J. Two-Dimensional Tantalum Disulfide: Controlling Structure and Properties via Synthesis. *2D Mater.* **2018**, *5*, 025001.
(38) Valencia-Ibáñez, S.; Jiménez-Guerrero, D.; Salcedo-Pimienta, J. D.; Vega-Bustos, K.; Cárdenas-Chirivi, G.; López-Manrique, L.; Herrera-Vasco, E.; Galvis, J. A.; Hernández, Y.; Giraldo-Gallo, P. Raman Spectroscopy of Few-Layers TaS2 and Mo-Doped TaS2 with Enhanced Superconductivity. *Adv. Electron. Mater.* **2022**, *8*, 2200457.
(39) Kovalska, E.; Roy, P. K.; Antonatos, N.; Mazanek, V.; Vesely, M.; Wu, B.; Sofer, Z. Photocatalytic Activity of Twist-Angle Stacked 2D TaS2. *NPJ. 2D. Mater. Appl.* **2021**, *5*, 68.
(40) Sugai, S. Effect of the Charge-Density-Wave Gap on the Raman Spectra in Orthorhombic Tas3. *Phys. Rev. B* **1984**, *29*, 953−965.
(41) Blagojević, J.; Mijin, S. D.; Bekaert, J.; Opačić, M.; Liu, Y.; Milošević, M. V.; Petrović, C.; Popović, Z. V.; Lazarević, N. Competition of Disorder and Electron-Phonon Coupling in 2H-TaSe2-x Sx ($0 \leq x \leq 2$) as Evidenced by Raman Spectroscopy. *Phys. Rev. Mater.* **2024**, *8*, 024004.
(42) Wu, Y.; Näther, C.; Bensch, W. Synthesis, Crystal Structure and Properties of K2Ta 2S10: A Novel Ternary Tantalum Polysulfide with TaS 8 Polyhedra Forming Infinite Anionic Chains. *J. Solid State Chem.* **2005**, *178*, 1569−1574.
(43) Joseph, C.; Bourson, P.; Fontana, M. D. Amorphous to Crystalline Transformation in Ta2O5 Studied by Raman Spectroscopy. *J. Raman Spectrosc.* **2012**, *43*, 1146−1150.
(44) Singh, B.; Wang, Y.; Liu, J.; Bazak, J. D.; Shyamsunder, A.; Nazar, L. F. Critical Role of Framework Flexibility and Disorder in Driving High Ionic Conductivity in LiNbOCl4. *J. Am. Chem. Soc.* **2024**, *146*, 17158−17169.
(45) Lei, M.; Li, B.; Liu, H.; Jiang, D. en. Dynamic Monkey Bar Mechanism of Superionic Li-Ion Transport in LiTaCl6. *Angew. Chem., Int. Ed.* **2024**, *63*, No. e202315628.
(46) Bloembergen, N.; Purcell, E. M.; Pound, R. V. Relaxation Effects in Nuclear Magnetic Resonance Absorption. *Phys. Rev.* **1948**, *73*, 679.
(47) Duchardt, M.; Neuberger, S.; Ruschewitz, U.; Krauskopf, T.; Zeier, W. G.; Auf Der Günne, J. S.; Adams, S.; Roling, B.; Dehnen, S. Superion Conductor Na11.1Sn2.1P0.9Se12: Lowering the Activation Barrier of Na+ Conduction in Quaternary 1−4-5−6 Electrolytes. *Chem. Mater.* **2018**, *30*, 4134−4139.
(48) Schlem, R.; Banik, A.; Ohno, S.; Suard, E.; Zeier, W. G. Insights into the Lithium Sub-Structure of Superionic Conductors Li3YCl6 and Li3YBr6. *Chem. Mater.* **2021**, *33*, 327−337.
(49) Jung, R.; Metzger, M.; Maglia, F.; Stinner, C.; Gasteiger, H. A. Oxygen Release and Its Effect on the Cycling Stability of LiNi x Mn y Co z O 2 (NMC) Cathode Materials for Li-Ion Batteries. *J. Electrochem. Soc.* **2017**, *164*, A1361−A1377.
(50) Li, X.; Liu, H.; Zhao, C.; Kim, J. T.; Fu, J.; Hao, X.; Li, W.; Li, R.; Chen, N.; Cao, D.; Wu, Z.; Su, Y.; Liang, J.; Sun, X. Hopping Rate and Migration Entropy as the Origin of Superionic Conduction within Solid-State Electrolytes. *J. Am. Chem. Soc.* **2023**, *145*, 11701−11709.
(51) Oliver, W. C.; Pharr, G. M. An Improved Technique for Determining Hardness and Elastic Modulus Using Load and Displacement Sensing Indentation Experiments. *J. Mater. Res.* **1992**, *7*, 1564−1583.
(52) Hempel, J. L.; Thapa, S.; Kim, K.; Kweon, K. E.; Wood, B. C.; Sevryugina, Y. V.; Mohtadi, R.; Tutusaus, O.; Cheng, Y. T. Probing the Elastic Modulus and Hardness of Superionic Boron Cluster Solid Electrolytes. *J. Power Sources* **2025**, *641*, 236800.
(53) Cho, Y. H.; Wolfenstine, J.; Rangasamy, E.; Kim, H.; Choe, H.; Sakamoto, J. Mechanical Properties of the Solid Li-Ion Conducting Electrolyte: Li 0.33 La 0.57 TiO 3. *J. Mater. Sci.* **2012**, *47*, 5970−5977.
(54) Hao, S.; Zhang, Q.; Kong, X.; Wang, Z.; Gao, X. P.; Shearing, P. R. Intrinsic Mechanical Parameters and Their Characterization in Solid-State Lithium Batteries. *Adv. Energy Mater.* **2025**, *15*, 2404384.

https://doi.org/10.1021/acsmaterialslett.5c01054
ACS Materials Lett. 2025, 7, 4029−4036